All-dielectric metasurface imaging platform applicable to laser scanning microscopy with enhanced axial resolution and wavelength selection

DASOL LEE,[1] MINKYUNG KIM,[1] JEONGHYUN KIM,[1] HYEONJUN HONG,[1] TREVON BADLOE,[1] DONG SUNG KIM,[1] AND JUNSUK RHO[1,2,*]

[1]*Department of Mechanical Engineering, Pohang University of Science and Technology (POSTECH), Pohang 37673, South Korea*
[2]*Department of Chemical Engineering, Pohang University of Science and Technology (POSTECH), Pohang 37673, South Korea*
[*]jsrho@postech.ac.kr

Abstract: Metasurfaces composed of artificially fabricated nano-sized structures have shown extraordinary potential for the precise control of light. Here, we demonstrate for the first time, a metasurface application to reduce the axial size of the point spread function in laser scanning microscopy. The all-dielectric metasurface has wavelength selectivity over the whole visible range, and confinement of the excitation point spread function of the electromagnetic field. These two unique features allow the metasurface to be applied to laser scanning microscope systems. Numerical and experimental demonstrations of the proposed all-dielectric metasurface are reported, showing sharp implicit spectral filtering in the visible range and enhanced axial confinement by observing actin filaments in NIH3T3 cells. We believe that our approach can provide a useful insight on the practicality of using metasurfaces as an imaging platform.

1. Introduction

Metasurfaces are planar optical elements composed of artificially fabricated nano-sized structures and have ability to precisely control optical properties. Metasurfaces have been utilized in holograms [1–8], color filters [9–12], beam steering devices [13–15], invisibility cloaks [16] and metalenses [17–21]. Metalenses show great potential for practical applications as an imaging platform. High numerical aperture (NA), aberration free, and broadband focusing metalenses may be able to replace conventional lenses in optical systems. However, recent work on metasurface-based imaging has focused only in metalenses, despite the axial light confinement and wavelength selection capabilities of the metasurface, which are of great benefit to optical imaging systems.

The confinement of light is required to increase the resolution of structures against background noise. Laser scanning (LS) based microscope systems like laser scanning confocal microscopy (LSCM) and stimulated emission depletion (STED) microscopy [22] offer higher signal-to-background noise ratio (SBNR) images than conventional wide-field microscopy because LS systems use a densely-focused excitation illumination light and a pinhole that can remove the out-of-focus noise. The axial excitation can also be restricted to the superficial layer by using total internal reflection [23] and plasmonics [24,25] because the evanescent field from those phenomena only affect the top 100 nm of samples. Optical interference has also been used to excite a thin layer along the axial direction, and thereby enhance the axial resolution. Various novel techniques to generate interference have been reported, including 4Pi microscopy [26], I[5]M microscopy [27], the mirror-enhanced axial resolution technique [28] and standing-wave

excitation microscopy [29]. These techniques effectively generate interference at the focal spot, but their delicate alignment processes and overall complexity of the systems obstruct their practical use.

Many fluorescence-based imaging systems use a laser as the light source due to its high output power and collimated beam focused in a diffraction-limited spot. However, lasers are monochromatic sources, so several lasers are required in combination to measure multiple fluorescence. This obstacle was cleared with the advent of supercontinuum sources [30], which provide white light emission along with high power and laser beam profiles. Many LSCM and STED imaging systems with a supercontinuum laser source have been reported [31–34] and commercialized. Although white laser sources achieve tunable color over the full range of visible light, they require electronically programmable devices to select the desired wavelength (λ). These are usually acousto-optical tunable filters (AOTF), which results in this being a cost-inefficient system. No effective solutions to replace the existing filter system has yet emerged.

Here, we propose a metasurface application that enables an imaging system with two functions; enhanced axial resolution of LSCM and implicit spectral filtering, providing new approaches to the aforementioned bottlenecks with a simple and applicable imaging platform. The metasurface is composed of an array of nano-sized hydrogenated amorphous silicon (a-Si:H) discs. It exhibits a sharp reflection spectrum which can be used to excite the target fluorochromes. The reflectance peak can be shifted by adjusting the unit structure of the dielectric metasurface, so the entire visible range can be covered. The metasurfaces are also optimized to create an axially-narrow excitation region. At the peak wavelength, reflected beams form interference patterns with the incident Gaussian beam, generating the excitation point spread function (PSF) near the metasurface, behind the specimen. This PSF is axially thin, and this dielectric metasurface-enhanced axial-narrowing imaging technique (MAIT) approximately doubles the axial resolution compared to conventional diffraction limited microscopy. The characteristics of the spectrally narrow reflectance and axially-narrow PSF are demonstrated with numerical and experimental results. Finally, we observed axially-enhanced images of biological cells stained with two fluorescent dyes. This is the first attempt of exploiting the axial resolution enhancement and wavelength selectivity of dielectric metasurfaces for imaging applications. Moreover, various nanopatterns such as nanopillar, hole array and other structures have attracted considerable interest in biology due to its effects on cellular responses like adhesion, cell motility and morphorlogy [35–38]. We believe that the engineering of nano-sized unit cell of dielectric metasurfaces can bring a significant advance in imaging areas, especially in observation of biomolecules on nanopatterned substrate with additional functionality like axially high SBNR and implicit filtering.

2. Proposed dielectric metasurface design

The concept of our approach is described in Fig. 1(a). The schematic diagram of MAIT is similar to conventional confocal scanning microscopy. The excitation laser is focused at the image plane through a high NA objective lens. The fluorescence emitted from the specimen is collected by the same objective lens and captured in the photo multiplier tube (PMT). The difference between MAIT and conventional systems is that the specimen is directly placed on the designed metasurface. For each measurement, the specimen should be prepared on a different metasurface due to the absence of the protecting layer in the current metasurface design. Also, there is no excitation filter in the path of excitation light due to the implicit spectral filtering of the metasurface. In the inset of Fig. 1(a), the details of MAIT are described. The Gaussian excitation light is illuminated onto the metasurface and reflected at a certain narrow range of wavelengths, which are determined by the design of the metasurface. The reflected light interferes with the excitation light, making an axially narrowed PSF away from the metasurface and the axially confined region is formed between the metasurface and cover glass. A small region (indicated with red ellipse) inside the specimen can excite the fluorescence with minimal axial volume.

Compared to conventional LSCM's axial resolution of 500 nm, MAIT shows a PSF of about half that value.
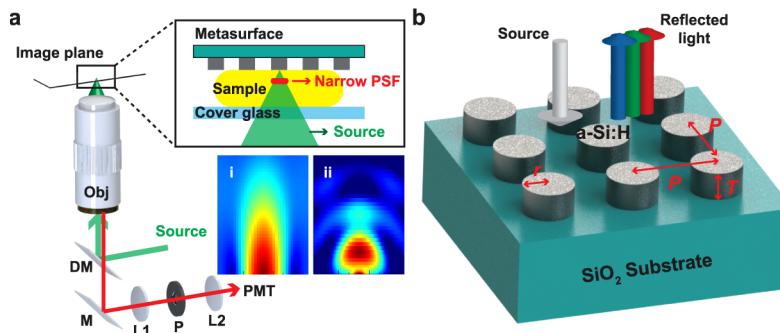

Fig. 1. (a) Schematic of MAIT. Source light is illuminated to the image plane, and the emitted fluorescence is captured by PMT through a pinhole and optics system (Obj: objective lens, DM: dichroic mirror, M: mirror, L1-L2: lenses, P: pinhole). The specimen is placed directly onto a dielectric metasurface with a-Si:H nanodiscs. Inset shows the magnified view of the black box. Constructive interference is formed inside the specimen with a small axial excitation region (red ellipse). The beam profile of the source light and narrow PSF is shown in the inset (i) and (ii), respectively. (b) Schematic of the designed dielectric metasurface. On an SiO_2 substrate, a-Si:H nanodiscs are arranged in an array with period P. Each nanodisc has radius r and thickness T. The metasurface selectively and efficiently reflects a narrow range of wavelengths.

A schematic of the all-dielectric metasurface is shown in Fig. 1(b). It is made up of an array of a-Si:H nanodiscs. Compared to a normal amorphous silicon which suffers from low efficiency in visible region, a-Si:H has relatively high refractive index and near-zero extinction coefficient in the visible regime due to hydrogen impurities. Thus, a-Si:H has low optical loss at visible wavelength (Appendix, Fig. 5). The unit structure has subwavelength dimensions of radius r, period P and thickness T. The reflection characteristics of the metasurface can be designed by choosing the appropriate structural parameters. In principle, a single dielectric nanodisc can support a Mie electric dipole and a magnetic dipole resonance. However, due to the low refractive index of the a-Si:H nanodiscs, these resonances are weak and cannot be easily distinguished from the reflected light of the substrate. The magnitude of the resonant modes can be increased by placing multiple nanodisc scatterers closely together. When the number of nanodiscs increases, the resonant mode is strengthened [39]. Therefore, a metasurface made up of a periodic array of a-Si:H nanodiscs can generate sufficient structural reflectance for MAIT. The geometry of the nanodiscs and their periodicity can be designed to tune the electric and magnetic dipole resonances for high reflection efficiency with a reduced full width at half maximum (FWHM) in the whole visible range.

3. Implicit spectral filtering and axially confined point spread function

To further explore the implicit spectral filtering of the metasurface, numerical analysis was performed using the finite-difference time-domain (FDTD) method to find the optimum parameters for sharp and high reflection. The calculated reflection is described in Fig. 2(a). High reflection peaks can be generated over a broad wavelength region, from 450 nm to 700 nm. Figure 2(b) shows the selected reflection graph in Fig. 2(a), and the peak is normalized for easier comparison. We observed that the peak is shifted to longer wavelengths when r is increased. For nanodiscs with T of 100 nm, the reflection peaks appear at 488 nm, 556 nm, 596 nm and 647 nm when r is 75 nm, 94 nm, 106 nm and 124 nm, and P is 334 nm, 379 nm, 408 nm and 442 nm, respectively.

The results show a narrow FWHM due to the effects of the periodic structure and the low loss of the dielectric material [39,40]. To prove the reflection of designed metasurface, we fabricated two metasurfaces, one with the highest peak at 488 nm and the other at 556 nm. Figures 2(c) and 2(d) show the measured reflection spectra of the fabricated metasurfaces (Appendix, Fig. 6) with an insert image of the reflected color. The measured reflectance of each metasurface at the resonance of 488 nm and 556 nm shows 0.41 and 0.63, respectively. Compared to the simulated reflectance of 0.42 and 0.66, the measured spectra and structural color response of the fabricated metasurfaces match well with the numerically calculated results. Our metasurfaces are based on Mie resonance, which accompanies the electric dipole (ED) and magnetic dipole (MD). For clear visualization, a metasurface with $r = 75$ nm and $P = 334$ nm is simulated to show the electric field profiles and current density at the resonance. Under the x-polarized illumination, ED and MD resonances occur at 488 nm simultaneously as shown in Fig. 2(e)–2(g). Whereas metallic nanopatterns exhibit ED resonance dominantly, the high index dielectric nanodiscs induce circulating current density as a result of phase retardation and field penetration. The circular displacement current in xz plane generates MD resonance along y-axis at the same
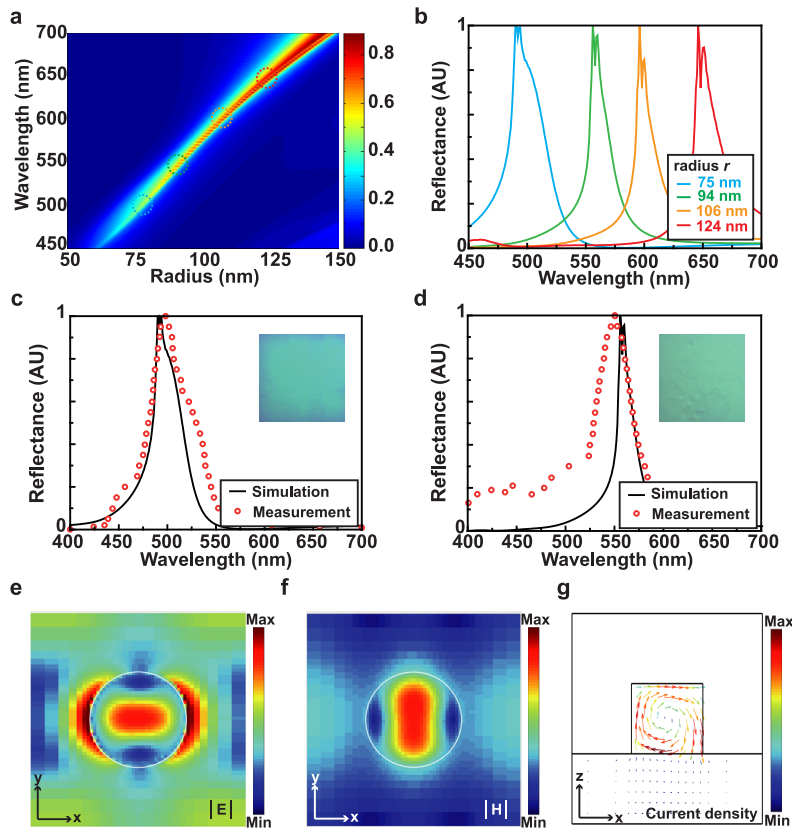
Fig. 2. (a) Reflection from the metasurface as affected by the nanodisc radius r and wavelength λ. An increase in r causes an increase in the λ that is reflected with high efficiency and a narrow FWHM. (b) Plots of normalized selected λ in Fig. 2(a). Each reflection spectrum shows a narrow bandwidth, which is selectively reflected at a desired λ. Simulated and measured reflection spectra of (c) $r = 75$ nm and (d) $r = 94$ nm. (e) Field profile for the ED resonance, (f) field profile for the MD resonance and (g) current density in xz plane at $\lambda = 488$ nm.

wavelength as shown in Fig. 2(f) and 2(g). The spectral overlap of the ED and MD inside the nanodisc brings out high and sharp reflection peak. We performed detailed parametric study to control the reflection (Appendix, Fig. 7).

The optimized metasurfaces were simulated to predict the axial confinement of the PSF. We simulated the excitation electromagnetic field for conventional confocal microscopy and MAIT. The simulation parameters were set to match the experimental and simulation details as described in the experimental section. The results of the electric field distribution in the y-z plane at different wavelengths of 488 nm, 556 nm, 596 nm and 647 are shown in Fig. 3(a)–3(d). The z-axis represents the distance from the top of the nanodiscs. MAIT shows tightly confined excitation PSFs, which have axial direction sizes of around 217 nm, 234 nm, 261 nm and 270 nm, respectively. Two counter-propagating Gaussian beams generate an interference pattern which can be used to confine light beyond the diffraction limit along the axial direction, which can increase the local electromagnetic field above the metasurface. Constructive and destructive interference occurs when the phase difference of the counter-propagating beams is 0 and π, respectively. The phase difference of the incident and reflected beams and the amplitude of the interference pattern along the propagation axis are described (Appendix, Fig. 8). The axially confined PSF is created at the positions where the two beams phases match and constructively interfere. The slight mismatch at 160 nm can be explained by the spatially varying amplitude of the reflected beam. In contrast to MAIT, the excitation PSF of conventional confocal microscopy (Fig. 3(e)) shows high electric field intensity around 500 nm along the z axis; i.e., objects placed closer than 500 nm cannot be resolved axially and SBNR is low due to the wide PSF. MAIT increases the axial resolution of LS microscopy around 1.85 to 2.30-fold depending on the wavelength. Compared to 4Pi microscopy, the confinement of PSF has a similar axial size. However, 4Pi has two sidelobes between the two faced objective lens, whereas MAIT has only one sidelobe that can
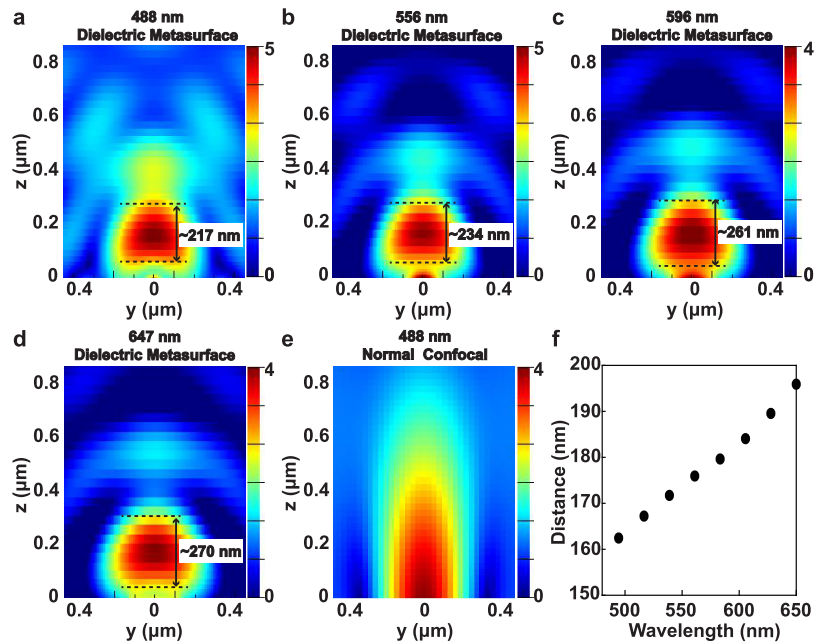
Fig. 3. Electric field amplitude profiles in the y-z plane of MAIT using metasurfaces that have reflection peaks at: (a) 488 nm, (b) 556 nm, (c) 596 nm and (d) 647 nm. (e) Normal confocal PSF at 488 nm. (f) Distance of PSF from the metasurface according to different wavelength.

acquire sharp images [41]. The distances between the confined fields of PSF and the metasurface are described in Fig. 3(f). The placement of PSFs near the metasurface is around 200 nm, but excitation light with longer wavelengths shows a PSF further away from the metasurface. TIRF microscopy [23] forms an excitation field close to the any glass cover. In contrast, due to the PSF existing near the metasurface, the existence of a glass cover above the specimen has no effect on the axial confinement of MAIT. Therefore, the sample thickness and glass cover position does not need to be considered. Some additional information about the spatial PSF characteristics with different background refractive index (Appendix, Fig. 9) are explained.

4. Cell imaging results

To verify the ability of imaging with the enhanced axial resolution of MAIT, the microstructures of NIH3T3 cells were observed. Optically-sectioned image quality can be dramatically sharpened when the axial resolution is enhanced by removing the signal from the out-of-excitation region. We applied MAIT in a commercial confocal microscope system and performed an imaging experiment to show high SBNR using two metasurfaces. The microscope had a 63X (NA = 1.3) oil-immersion objective lens and the captured fluorescence signal was properly cut by a mounted emission filter. The pinhole size was fixed to 1 AU and the laser power was fixed during the measurement. We can confirm that MAIT has a smaller PSF leading to an increased SBNR, and clearer images than conventional confocal microscopy.

Observing microstructures is crucial in investigations of intracellular structure. We stained the cells with red (λ_{ex}: 545 nm; λ_{em}: 570 nm) and green (λ_{ex}: 495 nm; λ_{em}: 520 nm) fluorescent dye to resolve layers of actin filaments, which are responsible for regulating cell shape and motility. The normal confocal images with different colors are shown in Fig. 4(a) and 4(d). Due to the large PSF in the excitation region, even though the focus is well formed on the sample plane, blurry background noise is captured simultaneously in the optical sectioning image. In contrast, the MAIT images with two metasurfaces in Fig. 4(b) and 4(e) show clear elliptical shadows of the nuclei that are distinct from the actin filaments, and the margins of the cell are more apparent compared to the normal confocal images. An axially thin section in the middle of the filaments is excited, while the top and bottom regions of the filaments are not, so they can easily be distinguished from the background signal. It demonstrates that a minimized PSF is well formed near the metasurfaces and the axial resolution is enhanced. The red and blue curves in Fig. 4(c) and 4(f) show the intensity along the dashed white lines in Fig. 4(a)–4(b) and 4(d)–4(e), respectively. The red lines are from normal confocal images and the blue lines are from MAIT. Numerically, the SBNR is increased about 1.75-fold when the ratio between the signal to background intensity is comparable in both cases. In the normal confocal image, the out-of-focus signal (yellow box) is captured simultaneously and makes the image blurred as shown in Fig. 4(g). In contrast, the MAIT images in Fig. 4(h)–4(i) show high contrast filaments images clearly. The normalized intensity profiles in Fig. 4(j), which show the thickness of single filament (yellow indicator) in Fig. 4(h)–4(i), prove that axial resolution enhancement can indirectly affect to the lateral resolution as well as the image contrast due to the high SBNR.

To achieve further axial resolution improvement, higher reflection at desired wavelength should be required. However, current design of metasurface used in MAIT shows less than 85 % reflectance in visible range. We examined the effect of reflection coefficient on the axial resolution enhancement by analytically calculating the interference of the incident and the reflected Gaussian beams (Appendix, Fig. 10). The axial resolution can be further enhanced by designing metasurfaces with high reflection peak at a desired wavelength.
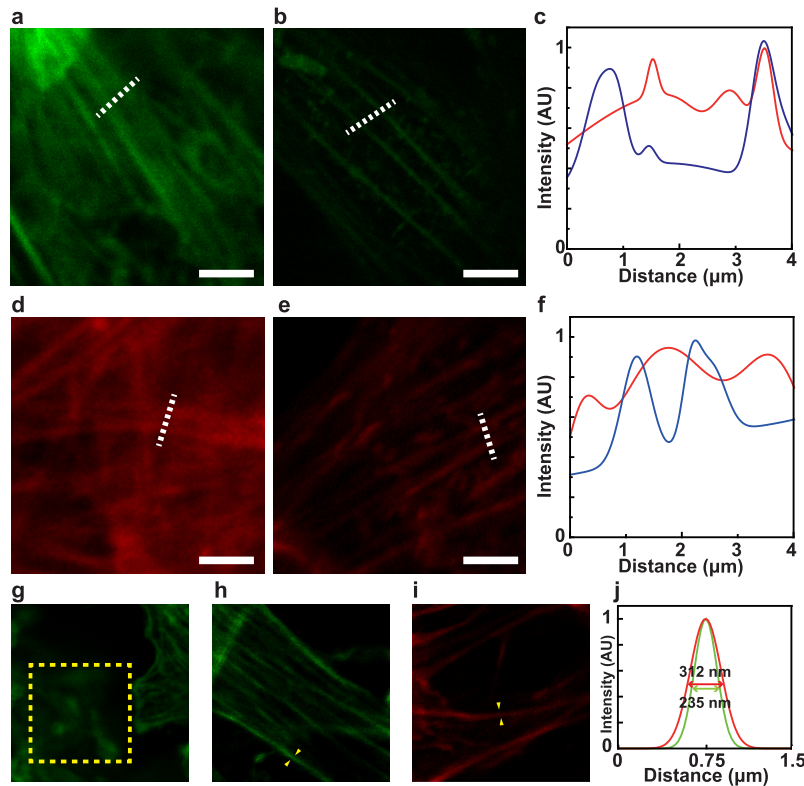
Fig. 4. NIH3T3 cell images of normal confocal microscopy and MAIT for comparison of normal confocal microscopy and MAIT. Captured cell image stained with green fluorescent dye from (a) the normal confocal microscopy and (b) MAIT. (c) Intensity profile of the dashed lines in Fig. 4(a)–4(b). Captured cell image stained with red fluorescent dye from (d) the normal confocal microscopy and (e) MAIT. (f) Intensity profile of the dashed line in Fig. 4(d)-(e), as in Fig. 4(c). The red and blue lines in Fig. 4(c) and 4(f) represent the fitted intensity profiles from normal confocal microscopy and MAIT, respectively. Scale bars are 5 μm. (g) Image obtained by normal confocal microscopy with out-of-focus signal, blurring the image. Cell images stained with (h) green and (i) red fluorescent dye are captured by MAIT with high SBNR and contrast. (j) Intensity profile of the yellow indicators showing single filament structure in Fig. 4(h) and 4(i).

5. Methods

5.1. Numerical modeling and simulation

Commercial FDTD software (Lumerical FDTD) was used for simulations. Reflection, impedance and effective refractive index spectra were simulated with periodic boundary conditions along the x axis and y axis, and a perfectly-matched layer (PML) along the z axis. The simulated reflection spectra were used to calculate other subset data (e.g., scaling factor, Q-factor). PSF profile simulation was performed with several a-Si: H structures. The length of each x and y plane was fixed to 8 λ and simulated with PML boundary conditions along the x, y and z axes. The Gaussian beam was approximated by a combination of 1,000 plane waves to produce NA 1.3, which is the same as the objective lens in the experiment.

5.2.　Fabrication

A 100 nm-thick layer of a-Si:H was deposited on a glass substrate by chemical vapor deposition (BMR Technology, HiDep-SC) with flow rates of SiH_4 10 sccm and H_2 75 sccm, RF power 800 W, and pressure 25 mTorr. A circle array composed of photoresist of poly (methyl methacrylate) (Microchem, 495 PMMA A2) was developed using methyl isobutyl ketone after standard EBL (ELIONIX, ELS-7800, 80 kV, 50 pA). A 30 nm chromium layer was deposited using an electron beam evaporator (KVT, KVE-ENS4004) and lifted-off. The a-Si:H was etched using a dry etcher (DMS, silicon/metal hybrid etcher). The remaining chromium mask was then removed using chromium etchant (CR-7).

5.3.　Cell preparation

The prepared sample was sterilized with 70 % ethanol for 5 min and rinsed with phosphate-buffered saline. The sample was placed inside a six-well cell culture plate and NIH3T3 fibroblast cells were seeded on the sample at a density of 1×10^6 cells/cm^2. The cells were cultured in a complete medium composed of high-glucose Dulbecco's Modified Eagle Medium (DMEM; Hyclone) supplemented with 10 % fetal bovine serum and 1 % penicillin/streptomycin. After 1 day of culture, the cells were fixed with 4 % paraformaldehyde at room temperature for 10 min, then permeabilized with 0.1 % Triton X-100 in PBS at 4 °C for 15 min. Then actin filaments of the cells in the samples were immunostained for 30 min with dyes that fluoresce in red (TRITC-conjugated phalloidin; Sigma) or green (FITC-conjugated phalloidin; Invitrogen). The immunofluorescence staining images of the actin filaments of the cells were obtained using a confocal microscope (ZEISS, LSM 700).

5.4.　Spectrum measurements

A lab-built spectrometer setup was used to obtain reflection spectra of metasurfaces. Unpolarized white light was beamed at the sample through the objective lens (10X, NA = 0.3), and the reflected light collected by the same objective lens. The captured reflected light was delivered to a spectrometer (IHR-320, Horiba) that has a CCD detector (Synapse CCD 1024 × 256, Horiba). Reflection spectra were normalized by the reflection measured from a silver mirror that has high reflectance in the visible range.

6.　Conclusion

In summary, we have proposed a method of combining all-dielectric metasurfaces with laser scanning microscopy to enhance the axial resolution with implicit spectral filtering. We found that the use of metasurfaces beneath the specimen can generate an interference-assisted axially confined layer away from the metasurface. Our all-dielectric metasurface provides spectral filtering at any wavelength in the whole visible range by adjusting the unit cell parameters. To practically prove this technique, actin filaments in NIH3T3 cells were distinguished clearly from background signal. We achieved a 2-fold axial resolution enhancement and a 1.75-fold SBNR enhancement in both simulation and experiment. To the best of our knowledge, this results have shown one-step advanced applicability in comparison with other techniques showing similar axial confinement effects. In addition to enhancing the axial resolution of the existing research, our method has additional advantages based on the designing of the nano-sized unit cells constituting the metasurface; spectral filtering and free designing of nanopatterns with proper structure parameters and optical characteristics. We expect that present MAIT will have an impact on imaging area as an useful imaging platform for observing cellular responses on patterned substrate by exploiting short axial depth and spectral filtering through the engineering of metasurfaces.
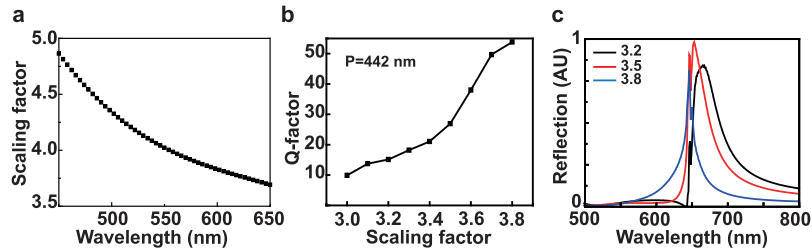
Appendix
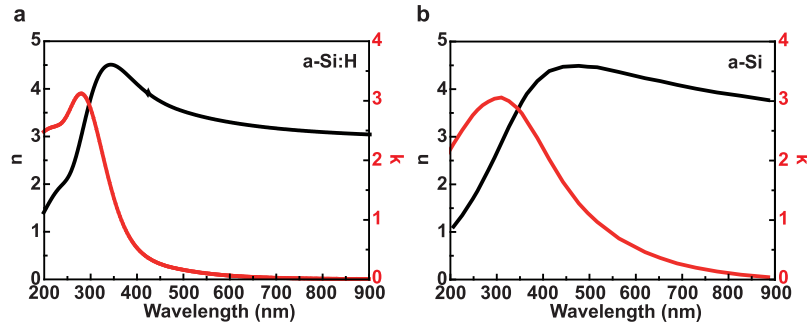
Fig. 5. Refractive index *n* (black lines) and extinction coefficient *k* (red lines) of: (a) a-Si:H and (b) a-Si.
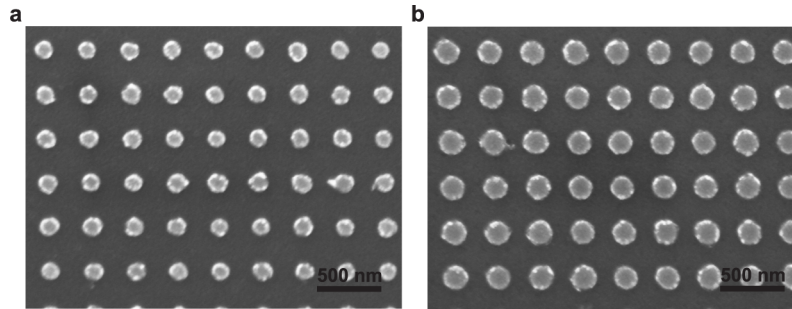

Fig. 6. SEM images of fabricated dielectric metasurfaces composed of a-Si:H nanodiscs array. Each metasurface has different geometrical parameters: (a) $r = 75$ nm, $P = 334$ nm, (b) $r = 94$ nm, $P = 380$ nm. PT was coated to acquire SEM images.


Fig. 7. (a) Scaling factor $F = P/r$ used in numerical simulation and fabrication. (b) Quality factor (Q-factor) when $P = 442$ nm, which yields a maximum reflectance peak at 647 nm. This term is considered to ensure that F sharpens the reflectance spectrum. The reflectance peak sharpens as the space between nanodiscs increases. (c) Reflectance spectra at $P = 442$ nm with $F = 3.2$, 3.5 and 3.8.
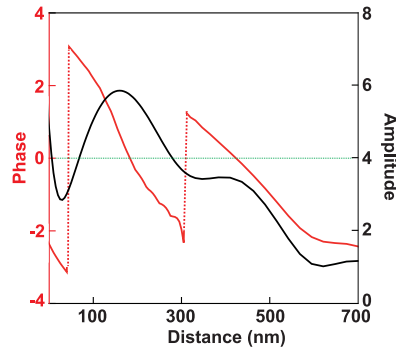
Fig. 8. The phase difference of the incident and the reflected beam (red) and amplitude of the interference pattern (black) along the propagation axis at wavelength of 488 nm.
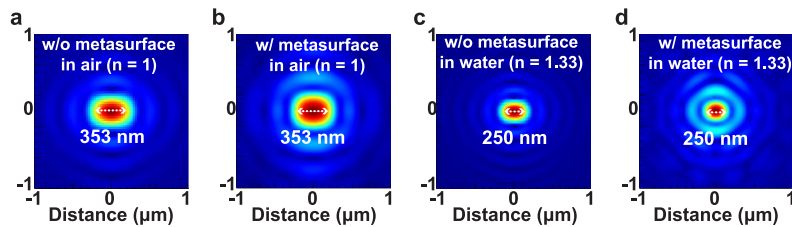
Fig. 9. Gaussian beam profiles on the x-y plane. (a) Normal Gaussian beam profile and (b) Gaussian beam profile on the metasurface. The refractive index of surrounding is 1 (air). (c) Normal Gaussian beam profile and (d) Gaussian beam profile on the metasurface. The refractive index of surrounding is 1.33 (water). The wavelength is 488 nm. As shown in the figures, there is no difference in spatial resolution. The Gaussian beam waist decreased when the surrounding refractive index increased.
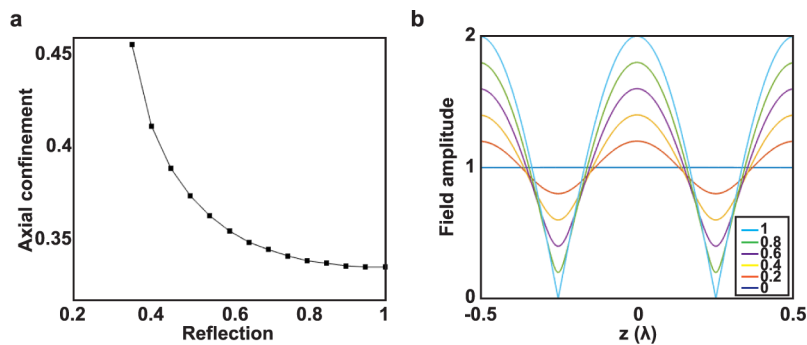
Fig. 10. (a) Axial confinement according to the reflection coefficient. (b) Field amplitude along the propagating axis. In the calculation, two Gaussian beams were illuminated along the propagation direction with opposite direction. One Gaussian beam is adjusted to have various amplitude which can be considered as the effective reflector having different reflection. The axial confinement is defined as a full-width half-maximum of the field amplitude in one cycle, normalized by wavelength.

Funding

References

1. B. Walther, C. Helgert, C. Rockstuhl, F. Setzpfandt, F. Eilenberger, E.-B. Kley, F. Lederer, A. Tünnermann, and T. Pertsch, "Spatial and spectral light shaping with metamaterials," Adv. Mater. **24**(47), 6300–6304 (2012).
2. L. Huang, X. Chen, H. Mühlenbernd, H. Zhang, S. Chen, B. Bai, Q. Tan, G. Jin, K.-W. Cheah, C.-W. Qiu, J. Li, T. Zentgraf, and S. Zhang, "Three-dimensional optical holography using a plasmonic metasurface," Nat. Commun. **4**(1), 2808 (2013).
3. X. Ni, A. V. Kildishev, and V. M. Shalaev, "Metasurface holograms for visible light," Nat. Commun. **4**(1), 2807 (2013).
4. L. Huang, H. Mühlenbernd, X. Li, X. Song, B. Bai, Y. Wang, and T. Zentgraf, "Broadband hybrid holographic multiplexing with geometric metasurfaces," Adv. Mater. **27**(41), 6444–6449 (2015).
5. G. Zheng, H. Mühlenbernd, M. Kenney, G. Li, T. Zentgraf, and S. Zhang, "Metasurface holograms reaching 80% efficiency," Nat. Nanotechnol. **10**(4), 308–312 (2015).
6. Z. Li, I. Kim, L. Zhang, M. Q. Mehmood, M. S. Anwar, M. Saleem, D. Lee, K. T. Nam, S. Zhang, B. Luk'yanchuk, Y. Wang, G. Zheng, J. Rho, and C.-W. Qiu, "Dielectric meta-holograms enabled with dual magnetic resonances in visible light," ACS Nano **11**(9), 9382–9389 (2017).
7. G. Yoon, D. Lee, K. T. Nam, and J. Rho, "Pragmatic metasurface hologram at visible wavelength: the balance between diffraction efficiency and fabrication compatibility," ACS Photonics **5**(5), 1643–1647 (2018).
8. G. Yoon, D. Lee, K. T. Nam, and J. Rho, ""Crypto-display" in dual-mode metasurfaces by simultaneous control of phase and spectral responses," ACS Nano **12**(7), 6421–6428 (2018).
9. J. Proust, F. Bedu, B. Gallas, I. Ozerov, and N. Bonod, "All-dielectric colored metasurfaces with silicon mie resonators," ACS Nano **10**(8), 7761–7767 (2016).
10. V. Flauraud, M. Reyes, R. Paniagua-Dominguez, A. I. Kuznetsov, and J. Brugger, "Silicon nanostructures for bright field full color prints," ACS Photonics **4**(8), 1913–1919 (2017).
11. Z. Dong, J. Ho, Y. F. Yu, Y. H. Fu, R. Paniagua-Dominguez, S. Wang, A. I. Kuznetsov, and J. K. Yang, "Printing beyond sRGB color gamut by mimicking silicon nanostructures in free-space," Nano Lett. **17**(12), 7620–7628 (2017).
12. S. Sun, W. Yang, C. Zhang, J. Jing, Y. Gao, X. Yu, Q. Song, and S. Xiao, "Real-time tunable colors from microfluidic reconfigurable all-dielectric metasurfaces," ACS Nano **12**(3), 2151–2159 (2018).
13. N. Yu, P. Genevet, M. A. Kats, F. Aieta, J.-P. Tetienne, F. Capasso, and Z. Gaburro, "Light propagation with phase discontinuities: generalized laws of reflection and refraction," Science **334**(6054), 333–337 (2011).
14. L. Huang, X. Chen, H. Mühlenbernd, G. Li, B. Bai, Q. Tan, G. Jin, T. Zentgraf, and S. Zhang, "Dispersionless phase discontinuities for controlling light propagation," Nano Lett. **12**(11), 5750–5755 (2012).
15. F. Aieta, M. A. Kats, P. Genevet, and F. Capasso, "Multiwavelength achromatic metasurfaces by dispersive phase compensation," Science **347**(6228), 1342–1345 (2015).
16. X. Ni, Z. J. Wong, M. Mrejen, Y. Wang, and X. Zhang, "An ultrathin invisibility skin cloak for visible light," Science **349**(6254), 1310–1314 (2015).
17. M. Khorasaninejad, W. T. Chen, R. C. Devlin, J. Oh, A. Y. Zhu, and F. Capasso, "Metalenses at visible wavelengths: Diffraction-limited focusing and subwavelength resolution imaging," Science **352**(6290), 1190–1194 (2016).
18. M. Khorasaninejad and F. Capasso, "Metalenses: Versatile multifunctional photonic components," Science **358**(6367), eaam8100 (2017).
19. F. Aieta, P. Genevet, M. A. Kats, N. Yu, R. Blanchard, Z. Gaburro, and F. Capasso, "Aberration-free ultrathin flat lenses and axicons at telecom wavelengths based on plasmonic metasurfaces," Nano Lett. **12**(9), 4932–4936 (2012).
20. D. Lin, P. Fan, E. Hasman, and M. L. Brongersma, "Dielectric gradient metasurface optical elements," Science **345**(6194), 298–302 (2014).
21. A. Arbabi, E. Arbabi, Y. Horie, S. M. Kamali, and A. Faraon, "Planar metasurface retroreflector," Nat. Photonics **11**(7), 415–420 (2017).
22. K. I. Willig, S. O. Rizzoli, V. Westphal, R. Jahn, and S. W. Hell, "STED microscopy reveals that synaptotagmin remains clustered after synaptic vesicle exocytosis," Nature **440**(7086), 935–939 (2006).
23. A. Trache and G. A. Meininger, "Total internal reflection fluorescence (TIRF) microscopy," Curr. Protoc. Microbiol. **10**, 2A–2 (2017).
24. R.-Y. He, G.-L. Chang, H.-L. Wu, C.-H. Lin, K.-C. Chiu, Y.-D. Su, and S.-J. Chen, "Enhanced live cell membrane imaging using surface plasmon-enhanced total internal reflection fluorescence microscopy," Opt. Express **14**(20), 9307–9316 (2006).
25. K. Kim, Y. Oh, K. Ma, E. Sim, and D. Kim, "Plasmon-enhanced total-internal-reflection fluorescence by momentum-mismatched surface nanostructures," Opt. Lett. **34**(24), 3905–3907 (2009).
26. S. W. Hell, S. Lindek, C. Cremer, and E. H. Stelzer, "Measurement of the 4Pi-confocal point spread function proves 75 nm axial resolution," Appl. Phys. Lett. **64**(11), 1335–1337 (1994).

27. M. G. Gustafsson, D. Agard, and J. Sedat, "I5M: 3D widefield light microscopy with better than 100nm axial resolution," J. Microsc. **195**(1), 10–16 (1999).
28. X. Yang, H. Xie, E. Alonas, Y. Liu, X. Chen, P. J. Santangelo, Q. Ren, P. Xi, and D. Jin, "Mirror-enhanced super-resolution microscopy," Light: Sci. Appl. **5**(6), e16134 (2016).
29. B. Bailey, D. L. Farkas, D. L. Taylor, and F. Lanni, "Enhancement of axial resolution in fluorescence microscopy by standing-wave excitation," Nature **366**(6450), 44–48 (1993).
30. S. Leon-Saval, T. Birks, W. Wadsworth, P. S. J. Russell, and M. Mason, "Supercontinuum generation in submicron fibre waveguides," Opt. Express **12**(13), 2864–2869 (2004).
31. D. Wildanger, E. Rittweger, L. Kastrup, and S. W. Hell, "STED microscopy with a supercontinuum laser source," Opt. Express **16**(13), 9614–9621 (2008).
32. R. Mercatelli, S. Soria, G. Molesini, F. Bianco, G. Righini, and F. Quercioli, "Supercontinuum source tuned by an on-axis monochromator for fluorescence lifetime imaging," Opt. Express **18**(19), 20505–20511 (2010).
33. K. Shi, P. Li, S. Yin, and Z. Liu, "Chromatic confocal microscopy using supercontinuum light," Opt. Express **12**(10), 2096–2101 (2004).
34. H. Kano and H.-O. Hamaguchi, "Vibrationally resonant imaging of a single living cell by supercontinuum-based multiplex coherent anti-stokes raman scattering microspectroscopy," Opt. Express **13**(4), 1322–1327 (2005).
35. S. Dobbenga, L. E. Fratila-Apachitei, and A. A. Zadpoor, "Nanopattern-induced osteogenic differentiation of stem cells–a systematic review," Acta Biomater. **46**, 3–14 (2016).
36. J. Lu, F. Zheng, Y. Cheng, H. Ding, Y. Zhao, and Z. Gu, "Hybrid inverse opals for regulating cell adhesion and orientation," Nanoscale **6**(18), 10650–10656 (2014).
37. L. C. Hsu, J. Fang, D. A. Borca-Tasciuc, R. W. Worobo, and C. I. Moraru, "Effect of micro-and nanoscale topography on the adhesion of bacterial cells to solid surfaces," Appl. Environ. Microbiol. **79**(8), 2703–2712 (2013).
38. S. Nasrollahi, S. Banerjee, B. Qayum, P. Banerjee, and A. Pathak, "Nanoscale matrix topography influences microscale cell motility through adhesions, actin organization, and cell shape," ACS Biomater. Sci. Eng. **3**(11), 2980–2986 (2017).
39. S. Sun, Z. Zhou, C. Zhang, Y. Gao, Z. Duan, S. Xiao, and Q. Song, "All-dielectric full-color printing with TiO_2 metasurfaces," ACS Nano **11**(5), 4445–4452 (2017).
40. Y. Shen, V. Rinnerbauer, I. Wang, V. Stelmakh, J. D. Joannopoulos, and M. Soljacic, "Structural colors from Fano resonances," ACS Photonics **2**(1), 27–32 (2015).
41. J. Bewersdorf, R. Schmidt, and S. W. Hell, "Comparison of I5M and 4Pi-microscopy," J. Microsc. **222**(2), 105–117 (2006).